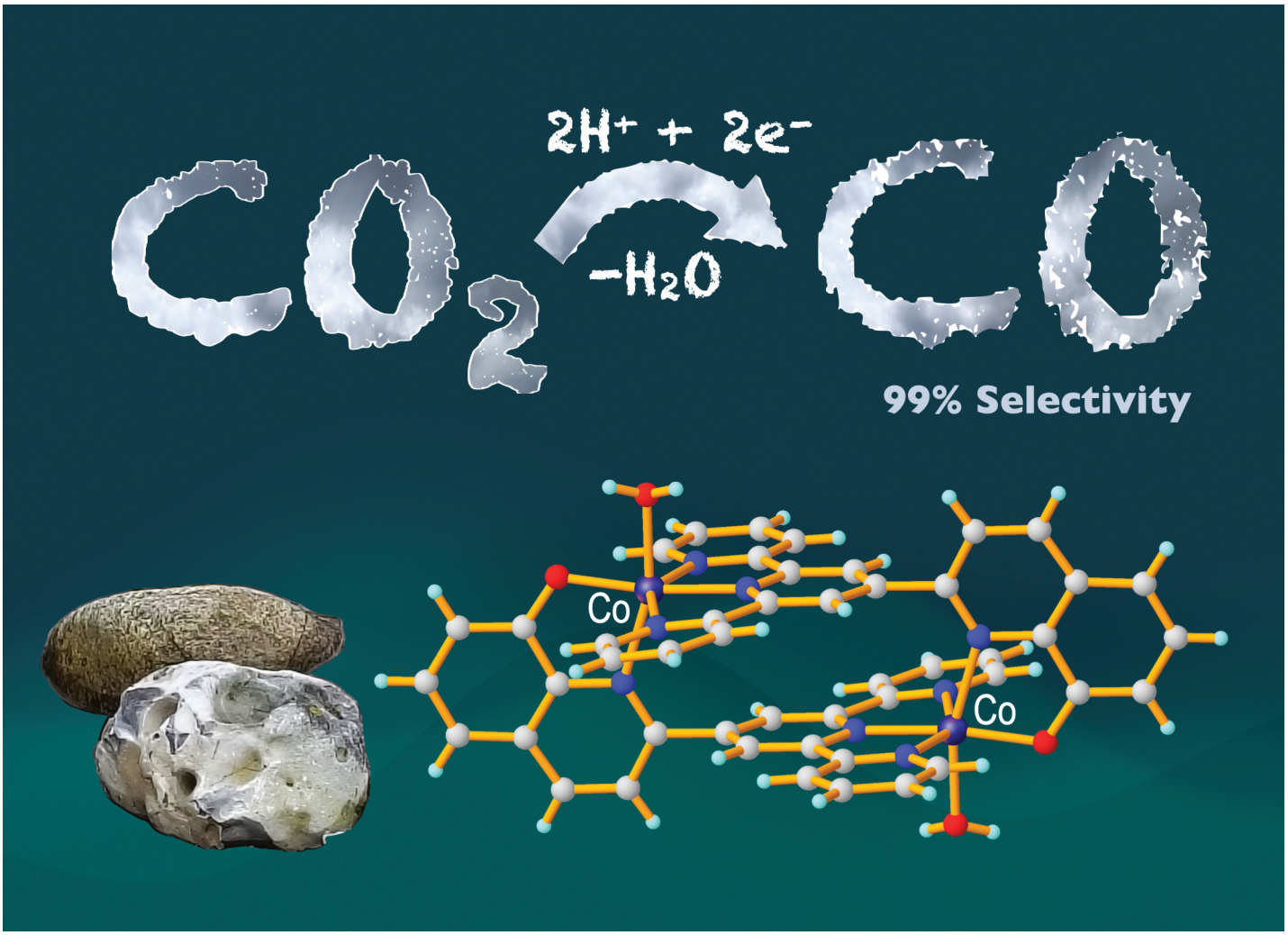

Showcasing research from Professor Sumanta Kumar Padhi's Artificial Photosynthesis laboratory, Department of Chemistry and Chemical Biology, Indian Institute of Technology (Indian School of Mines) Dhanbad, Jharkhand, INDIA.

Selective electrochemical CO_2 reduction to CO by a Co(II) dimer catalyst by metal–ligand cooperativity

Electrochemical CO_2 reduction offers a promising route to mitigate greenhouse gas emissions. We report a cobalt dimer catalyst that selectively converts CO_2 to CO in DMF/H_2O (4.8 : 0.2 v/v) with 94 ± 2% Faradaic efficiency, 99% selectivity, and TOF_{max} = 2575 s^{-1} at a 760 mV overpotential. Mechanistic studies (DFT, IR-SEC, KIE) reveal ECEC and EECC pathways involving stepwise proton–electron transfer and metal–ligand cooperativity. Reduction-induced ligand protonation enables CO_2 activation, providing mechanistic insights for designing advanced CO_2-to-CO molecular electrocatalysts.

Image reproduced by permission of Sumanta Kumar Padhi from *Dalton Trans.*, 2025, **54**, 16682.

As featured in:

See Sumanta Kumar Padhi *et al.*, *Dalton Trans.*, 2025, **54**, 16682.

ROYAL SOCIETY OF CHEMISTRY

rsc.li/dalton

Registered charity number: 207890

Dalton Transactions

ROYAL SOCIETY OF CHEMISTRY

PAPER

View Article Online
View Journal | View Issue

Cite this: *Dalton Trans.*, 2025, **54**, 16682

Selective electrochemical CO_2 reduction to CO by a Co(II) dimer catalyst by metal–ligand cooperativity

Sk Samim Akhter,[a] Koushik Makhal,[b] Dev Raj,[a] Manaswini Raj,[a] Thillai Natarajan M,[a] Bhabani S. Mallik,[b] Prabhakar Bhardwaj,[c] Pankaj Kumar,[c] Ebbe Nordlander[d] and Sumanta Kumar Padhi *[a]

An approach to reducing greenhouse gas emissions that shows promise is the electrochemical conversion of CO_2 to products with added value. Here, we present $[Co(8HQ\text{-}Tpy)(H_2O)]_2(PF_6)_2$ (**[Co1]**), a cobalt-based molecular electrocatalyst that can convert CO_2 to CO in a DMF/H_2O mixture (4.8 : 0.2 v/v) in a selective manner (8HQ-Tpy = 2-([2,2′:6′,2″-terpyridin]-4′-yl)quinolin-8-ol). At an overpotential of 760 mV, the catalyst shows a TOF_{max} of 2575 s^{-1} and a high Faradaic efficiency of 94 ± 2%. The CO_2 reduction follows both ECEC and EECC-type routes, involving stepwise proton and electron transfer, according to a mechanistic investigation that combines DFT calculations, infrared spectroelectrochemistry (IR-SEC), and kinetic isotope effect (KIE) observations. Sequential protonation and CO_2 activation are made possible by the reduction of a hexa- to penta-coordinate Co centre. According to DFT studies, protonation at the ligand O^- site, which takes place before CO_2 coordination and favours an EECC pathway, becomes thermodynamically favourable following reduction. Both deprotonated and protonated CO_2-derived intermediates are captured by IR-SEC measurements, and proton transfer is not rate-limiting as the KIE is low (k_H/k_D = 1.17). When taken as a whole, these results offer a comprehensive mechanistic understanding of CO_2-to-CO conversion as well as design guidelines for creating advanced molecular electrocatalysts for carbon capture and utilization.

Received 21st August 2025,
Accepted 21st October 2025

DOI: 10.1039/d5dt02003d

rsc.li/dalton

Introduction

Carbon dioxide is a greenhouse gas produced mainly from fossil fuel combustion. Over the last century, anthropogenic CO_2 emissions have increased alarmingly along with associated concerns, including climate change, rising sea levels and ocean acidification.[1–3] Increased atmospheric CO_2 concentration and the use of fossil resources are crucial factors of global environmental problems but effective technologies that convert CO_2 into sustainable fuels can mitigate such environmental issues.[4–6] In this context, electrochemical CO_2 reduction is extensively investigated to convert environmental CO_2 into fuels and value-added chemicals such as CO, HCOOH, CH_4, CH_3OH, C_2H_5OH, or higher molecular weight hydrocarbons.[7–9] Carbon monoxide is an essential industrial building block for acetic acid synthesis *via* the Monsanto process as well as aldehyde production using alkenes and H_2 by the hydroformylation reaction. Furthermore, a mixture of H_2 and CO (syngas) is utilized in Fischer-Tropsch catalysis to synthesize straight-chain alkanes, ideal for diesel fuel.[10–13] Homogeneous electrocatalytic CO_2 and proton reduction is being extensively explored to achieve reaction selectivity and to serve as a mechanistic model for improved large-scale CO_2 electroreduction processes.[14–19]

Transition-metal complexes are uniquely suited as catalysts for CO_2 reduction because they can store and transfer various electrons, thus circumventing the high-energy CO_2 radical intermediate. Numerous molecular catalysts based on transition metal complexes have been proposed for CO_2 reduction, generally exhibiting good product selectivity.[20–22] However, a significant challenge is that the reduction of CO_2 is kinetically restrained by multiple electron-transfer processes accompanied by the highly competitive hydrogen evolution reaction. Molecular catalysts based on Ru, Ir, Pd, and Re have been investigated for converting CO_2 to CO and formate. Catalysts based on earth-abundant transition metals,[23–25] such

[a]*Artificial Photosynthesis Laboratory, Department of Chemistry and Chemical Biology, Indian Institute of Technology (Indian School of Mines), Dhanbad, 826004, India. E-mail: sumanta@iitism.ac.in*
[b]*Department of Chemistry, Indian Institute of Technology Hyderabad, Sangareddy, 502284 Telangana, India*
[c]*Department of Chemistry, Indian Institute of Science Education and Research (IISER), Tirupati 517507, India*
[d]*Chemical Physics, Department of Chemistry, Lund University, Box 124, SE-221 00 Lund, Sweden*

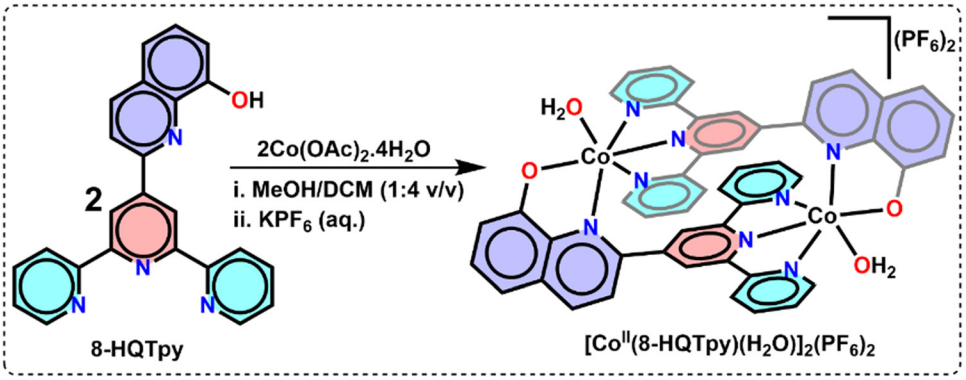

Scheme 1 A schematic depiction of the synthetic route to the $[Co^{II}(8HQ\text{-}Tpy)(H_2O)]_2(PF_6)_2$ **[Co1]** complex.

as Fe, Co, and Ni, could provide inexpensive materials for large-scale use.[26,27] However, such base metal catalysts are relatively labile and prone to generating H_2, resulting in low selectivity for CO_2 reduction. Redox-active ligands with extensive π–π conjugation can facilitate electron transfer and storage, thus accelerating electrocatalytic kinetics. Cobalt complexes with redox-active ligands prefer to reduce CO_2 to CO.[28–31] Several molecular cobalt-based catalysts with well-defined coordination environments have been reported for CO_2 reduction. Also, polypyridine ligands, represented by, *inter alia*, bipyridine (bpy) and terpyridine (tpy), have gained recognition for their inherent stability and ability to facilitate these electrochemical reduction of CO_2 in organic solvents. Elgrishi and collaborators focused on synthesizing $[Co(tpy)_2]^{2+}$ complexes and thoroughly examined their electrochemical properties. Their electrochemical investigations were conducted in an electrolyte consisting of 0.1 M $[NBu_4](ClO_4)$ dissolved in DMF. The findings from the electrochemical studies revealed the generation of CO and H_2 with Faradaic efficiencies ranging from 16% (CO) to 21% (H_2).[32] Later, the same group explored the potential of $[Co(tpy)_2]^{2+}$ to enhance CO generation despite its initially low Faradaic efficiency. The study involved comprehensive electrochemical analyses of the $[Co(tpy)_2]^{2+}$ and $[Co(tpyY_2X)_2]^{2+}$ systems, where substituents X, such as C_6H_5Cl, $C_6H_5CH_3$, H, OCH_3, and C_4H_9, were examined alongside Y, which could be H or C_4H_9. The primary reaction products observed were CO and H_2, with the substituents dictating the pathway of the reaction.[33]

In the endeavour to achieve efficient CO_2 reduction catalysis, cooperative reactivity between two metal centers has emerged as a feasible strategy for enhancing the catalytic effectiveness of molecular catalysts. When compared to single-metal counterparts, complexes comprising bimetallic Ni,[34] Fe,[35] Co,[36–38] Pd,[39] and Re[40,41] centers have shown modest to considerable improvements in catalytic rates and turnover numbers for CO_2 reduction. Cobalt dimer complexes have shown promise in CO_2 reduction due to their ability to facilitate multi-electron transfer steps and stabilize reactive intermediates.[36–38]

As demonstrated by Ni–Fe carbon monoxide dehydrogenases (CODHs), which accomplish reversible CO_2-to-CO conversion through spatial and functional cooperation between two metals, nature commonly uses bimetallic active sites to mediate challenging multielectron reactions.[7,34] This inspired us to employ a unique ligand 2-([2,2′:6′,2″-terpyridin]-4′-yl)quinolin-8-ol (8HQ-Tpy, Scheme 1) to create a fully bridged bimetallic cobalt complex, motivated by this biological precedent. In the present study, we have synthesized a novel and robust cobalt dimer complex $[Co(8HQ\text{-}Tpy)(H_2O)]_2(PF_6)_2$ **[Co1]** designed explicitly for electrochemical CO_2 reduction. In this architecture, the ligand acts as a structural and electronic scaffold, coordinating both cobalt centers through the quinoline and terpyridine moieties to establish octahedral coordination environments at each metal. The rigid 8HQ backbone, serves not only as a chelating unit, but also introduces asymmetry by bridging the second Co center. This system shows weak antiferromagnetic coupling (*vide infra*), indicating little electronic communication, in contrast to enzymatic systems where high metal–metal cooperativity directly catalyzes the reaction. Rather, metal–ligand cooperativity, in which the ligand promotes substrate binding, electron delivery, and geometric control, appears to be the source of the catalytic performance, especially the excellent selectivity for CO over H_2. By using this method, we can investigate how carefully crafted ligand frameworks can be used to tune activity and selectivity in molecular CO_2 reduction in place of direct M–M synergy.

Experimental section

Materials and methods

All chemicals, including 2-acetylpyridine, selenium dioxide (Tokyo Chemicals), ammonium hydroxide, KOH (Finar), and HPLC-grade DMF (Merck), were used without further purification. Ultrapure water was obtained from a Milli-Q system. Detailed procedures are provided in the SI.

Instrumentation

UV-Vis spectra were recorded on an Agilent Cary 8454 spectrophotometer; HRMS on a Waters XEVO G2-XS QTOF mass spectrometer; NMR (^1H and ^{13}C) on a Bruker 400 MHz spectro-

meter; and SCXRD on a Rigaku SuperNova diffractometer. Magnetic measurements were performed using a Quantum Design MPMS SQUID magnetometer. Electrochemical studies used a CHI 1140C system with Saturated Calomel Electrode, Pt wire, and glassy carbon electrodes. FT-IR, FESEM, and EDX data were collected using PerkinElmer Spectrum Two, Carl Zeiss Supra 55, and PHI 500 Versa Probe III instruments, respectively. Gas chromatography was performed on a Kshama 1310RJ GC with FID and TCD detectors. Additional details are available in the SI. Infrared spectroelectrochemical (IR-SEC) studies were conducted using a high-sealing, optically transparent thin-layer electrochemical (OTTLE) cell equipped with CaF_2 windows (Fig. S1).

Synthesis. $[Co(8HQ\text{-}Tpy)(H_2O)]_2(PF_6)_2$; [Co1]

The ligand (8HQ-Tpy) and the complex **[Co1]** were synthesized using the reported procedure for an analogous manganese complex.[42a] A methanolic suspension containing one equivalent of $Co(CH_3COO)_2{\cdot}4H_2O$ (66 mg, 0.21 mmol) was gradually added dropwise to a 25 mL of mixed solution consisting of CH_3OH and CH_2Cl_2 (in a ratio of 1 : 4, v/v) containing one equivalent of the ligand 8HQ-Tpy (0.1 g, 0.21 mmol). The reaction mixture was stirred at room temperature for 4–5 hours, after which the solvents were removed under vacuum to reduce the volume. An aqueous solution of KPF_6 was then added, resulting in the formation of an orange-red precipitate (Scheme 1). The precipitate was isolated from the reaction solution by reducing the volume under vacuum, then washing with ice-cold methanol and diethyl ether. Brown-coloured single crystals were obtained through slow evaporation of a DMF solution of the complex, yielding 55% with respect to the Co starting material. The isolated crystals of **[Co1]** were further analysed by single crystal X-ray diffraction. The UV-Visible spectrum and high-resolution mass spectrum of the obtained complex are depicted in Fig. S2 and S3. The calculated mass for $[Co_2C_{48}H_{30}N_8O_2]^{2+}$ was determined to be 434.058, while the found mass was 434.070.

Results and discussion

UV–Visible spectra and mass spectra

The absorption spectra of both ligand 8HQ-Tpy and complex **[Co1]** were examined in the organic solvent *N*,*N*-dimethyl formamide. The ligand 8HQ-Tpy exhibits two peaks at λ_{max} = 320 nm (ε = 15600 M^{-1} cm^{-1}) due to n–π^* transition(s) and another at λ_{max} = 371 nm (ε = 2700 M^{-1} cm^{-1}) corresponding to a CT (Charge Transfer) (Fig. S2(A)). A bathochromic shift due to the electron donating ability of 8HQ-Tpy was noted in the UV-Visible spectrum of **[Co1]**, corresponding to an ILCT-based peak (ILCT = Intra-Ligand Charge Transfer) at λ_{max} = 412 nm (ε = 7000 M^{-1} cm^{-1}) as shown in Fig. S2(B). The complex **[Co1]** exhibits a MLCT (Metal to Ligand Charge Transfer) band at λ_{max} = 490 nm (ε = 4200 M^{-1} cm^{-1}). Moreover, the UV-Vis spectrum of **[Co1]** also exhibits a broad low intensity d–d transition band centered at λ_{max} = 736 nm (ε = 170 M^{-1} cm^{-1}; Fig. S2(B)). The strong ILCT within the 8HQ-Tpy ligand framework diminishes the peak intensity of the d–d transition band at λ_{max} = 736 nm. The mass spectra of **[Co1]** recorded in DMF are shown in Fig. S3.

Single crystal X-ray analysis

Single crystals of the complex $[Co(8HQ\text{-}Tpy)(H_2O)]_2(PF_6)_2$ **[Co1]** were grown from a DMF solution. In order to elucidate the molecular structure of the complex, the crystal structure was determined by X-ray diffraction. The $[Co(8HQ\text{-}Tpy)(H_2O)]_2(PF_6)_2$ complex crystallizes in a monoclinic *C*2/*c* space group. The crystal data and refinement parameters are listed in Table S1. Selected bond distances and angles are tabulated in Tables S2 and S3. A solvent mask was applied, revealing one void per unit cell with a volume of 284 $Å^3$ containing approximately 72 electrons. This is consistent with the presence of one methanol (CH_4O) molecule per formula unit, accounting for 72 electrons per unit cell. The molecular structure of $[Co(8HQ\text{-}Tpy)(H_2O)]_2(PF_6)_2$ **[Co1]** is shown in Fig. 1. In the **[Co1]** dimer, the 8-HQ fragment of the 8HQ-Tpy ligand in one [Co(8HQ-Tpy)] moiety coordinates to the cobalt ion of the second moiety (Fig. 1). The first coordination sphere of each cobalt ion has a distorted octahedral geometry. Each individual cobalt center has a *mer*-[Co(NNN)(NOO′)] coordination geometry (NOO′: NO due to 8-HQ and O′ due to H_2O), with the plane of the tpy unit of the ligand nearly perpendicular (86.9°) to the plane generated by the 8-hydroxyquinoline (8-HQ) ligand fragment and the H_2O ligand (Fig. S4). The two cobalt(II) metal centers are separated from each other by a distance of approximately 6.98 Å. The compact intermolecular coordination contains a strong π···π interaction of *ca.* 3.39 Å (Fig. 1(C)). The Co1–N1 (2.144(2) Å) and Co1–N3 (2.145(2) Å) distances are approximately the same, while Co1–N2 (2.093(2) Å) is shorter than the Co1–N1 and Co1–N3 distances. The distortions observed in terpyridine complexes of first-row transition metals are due to a more efficient overlap of metal t_{2g} orbitals with the π^* orbitals of the central pyridyl group than the other two pyridyl rings (Fig. 1(C) and (D)).[42b–f]

The Co1–N4 bond length (2.214 (2) Å) by the 8-HQ fragment is longer than the Co1–N_{Tpy} bond distances. The Co1–O2 (2.136(2) Å) for the coordinated aqua ligand is significantly longer than the Co1–O1 bond (1.965(2) Å) involving the deprotonated oxygen of the 8-HQ moiety, which is the shortest bond in the cobalt coordination sphere. Among the three five-membered bite-angles, the ∠N2Co1N angles (∠N2Co1N3 (74.99(7)°), ∠N2Co1N1 (74.66(7)°)) generated by the Tpy moiety are more constrained than ∠N4Co1O1 (79.26(7)°) generated by the 8-HQ moiety.

Solid state magnetic properties

Magnetic susceptibility data for a solid sample of $[Co(8HQ\text{-}Tpy)(H_2O)]_2(PF_6)_2$ **[Co1]** was collected in the temperature span 10–300 K at 1000 Oe. Diamagnetic corrections were applied to calculate the magnetic susceptibility. The μ_{eff} value was found to be 7.88 at room temperature for the dimer (3.94 per cobalt centre). The exchange interactions between the two

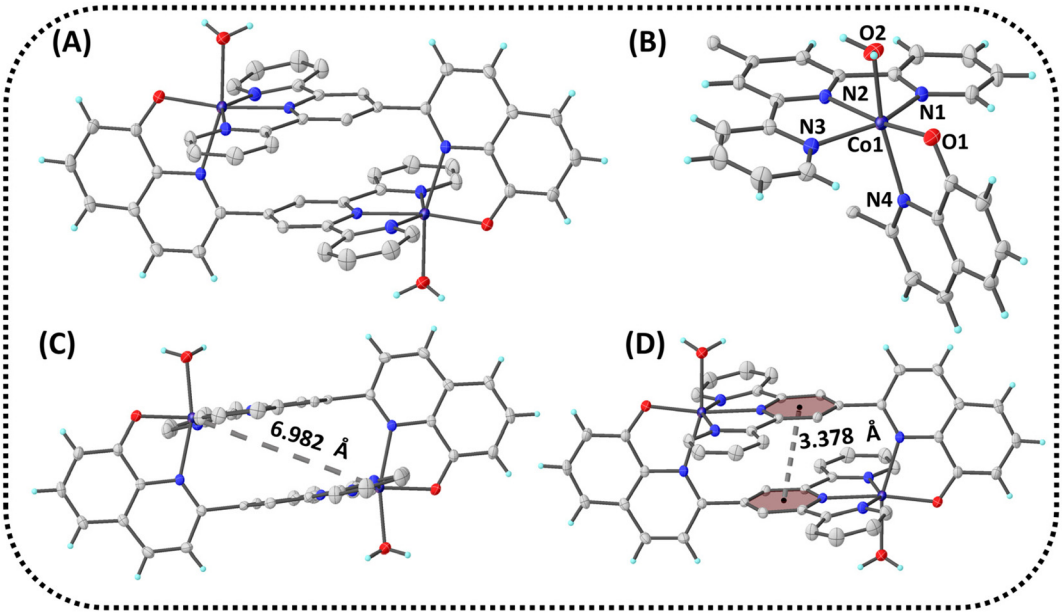

Fig. 1 (A) A thermal ellipsoid plot generated by Olex 2 software for $[Co(8HQ\text{-}Tpy)(H_2O)]_2^{2+}$ (some hydrogen atoms are omitted for clarity). (B) A partial plot shows that each Co ion has distorted octahedral geometry. (C) The shortest Co···Co distance, and (D) π···π interaction in **[Co1]**.

Co(II) centers were analysed considering isotropic and anisotropic interactions. In agreement with the crystallographically determined structure, the homo-dinuclear high-spin $[Co^{II}(8HQ\text{-}Tpy)(H_2O)]_2(PF_6)_2$ **[Co1]** complex was considered to possess an axially distorted octahedral coordination geometry for the anisotropic interactions. The magnetic susceptibility data were modeled using eqn (1), which accounts for anisotropic interactions between two high-spin Co(II) centers. The fitting was performed with MagSaki software, using the independent parameters J (exchange interaction), κ (orbital reduction factor), λ (spin–orbit coupling constant), and ν (distortion parameter, defined as $\Delta/\kappa\lambda$).[42g–i] The best-fitting parameters reveal a weak antiferromagnetic interaction with a coupling constant of $J = -1.1$ cm^{-1} between the two Co(II) centers. The orbital reduction factor ($\kappa = 0.93$) is equivalent to a free Co(II) center ($\kappa = 0.93$) (Fig. 2). The spin–orbit coupling parameter, $\lambda = -173$ cm^{-1}, is equivalent to a free ion Co(II) spin–orbit coupling parameter. The distortion parameter 'ν' was found to be −0.1, which indicates that the distortion is negligible.

$$\chi_A = \frac{\chi_z + 2\chi_x}{3} \quad (1)$$

where, $\chi_z = N\frac{F_1}{F_2}$ and $\chi_x = N\frac{F_3}{F_2}$ (N = Avogadro's number; F_1, F_2 and F_3 are the parameters used in ref. 42*e–g*).

In addition, the magnetic susceptibility data were fitted using a model consisting of homo-dinuclear high-spin cobalt (II) octahedral complexes with little distortion. The magnetic susceptibility was estimated using the Sakiyama susceptibility equation based on the model outlined in ref. 42*j–k*. A weak antiferromagnetic interaction, $J = -1.0$ cm^{-1} was also found in this case, with the κ and λ values equivalent to a free Co(II) ion (Fig. S5).

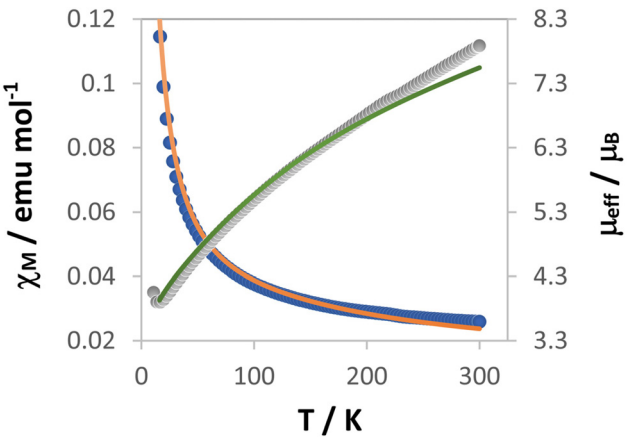

Fig. 2 The χT *vs.* T and χ *vs.* T plots for $[Co(8HQ\text{-}Tpy)(H_2O)]_2(PF_6)_2$; **[Co1]**. (Fitting parameters were $J = -1.113$ cm^{-1}, $\lambda = -173$ cm^{-1}, $\kappa = 0.93$, $\nu = -0.1$, $g = 2.0$, TIP = 12.9×10^{-3}, $R_\chi = 4.9 \times 10^{-3}$, $R_\mu = 5.5 \times 10^{-4}$.)

Electrochemistry

The redox behaviour of **[Co1]** and the ligand 8HQ-tpy was investigated using cyclic voltammetry (Fig. 3). The experiment was conducted in dry DMF, with 0.1 M $[NBu_4](ClO_4)$ as the supporting electrolyte under an inert atmosphere at ambient temperature. The ligand itself exhibited an irreversible redox wave at $E_c = -2.0$ V *vs.* $Fc^{+/0}$ and $E_a = -1.56$ V *vs.* $Fc^{+/0}$ and a quasi-reversible peak at $E_{cat/2} = -2.3$ V *vs.* $Fc^{+/0}$ (Fig. 3(A)).

The cyclic voltammogram revealed three metal-centered and three ligand-centered redox couples of the **[Co1]** complex.

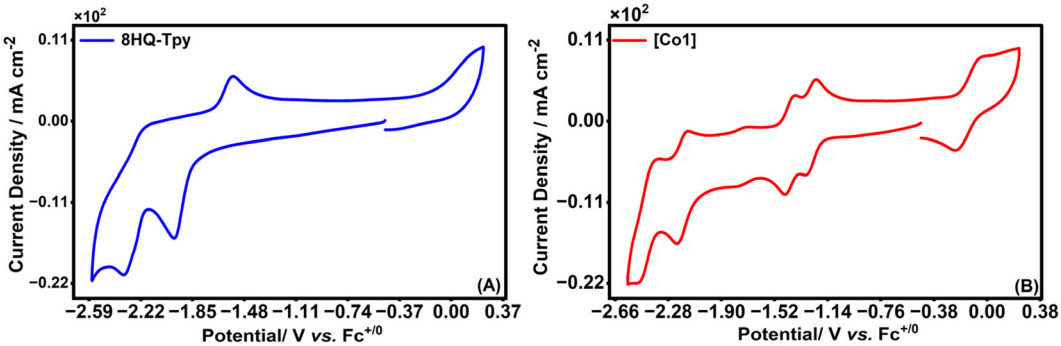

Fig. 3 Cyclic voltammograms in dry DMF using 0.1 M $[NBu_4](ClO_4)$ as a supporting electrolyte under N_2 atmosphere of 1.0 mM of (A) ligand 8HQ-Tpy (B) 1.0 mM of **[Co1]** complex.

Fig. 3(B) depicts a quasi-reversible wave at $E_{1/2}$ = −0.14 V *vs.* $Fc^{+/0}$; Fig. S6(D), assigned to the $Co^{III}Co^{III}/Co^{II}Co^{II}$ redox couple. The broad nature of this peak was attributed to the large reorganization energy involved in the transition between $Co^{II}Co^{II}$ and $Co^{III}Co^{III}$ redox states, corresponding to high spin d^7 to low spin d^6 configurations, respectively.[42d-f] It seems that both the Co^{II}-centres in **[Co1]** oxidise simultaneously to Co^{III}, and this was verified by chronoamperometry at E_{app} = +0.33 V *vs.* $Fc^{+/0}$ (Fig. S7(A) and S7(B)). Furthermore, the **[Co1]** complex exhibits other metal-based quasi-reversible peaks at $E_{1/2}$ = −1.26 V *vs.* $Fc^{+/0}$ and $E_{1/2}$ = −1.41 V *vs.* $Fc^{+/0}$ which were attributed to $Co^{II}Co^{II}/Co^{II}Co^{I}$ and $Co^{I}Co^{II}/Co^{I}Co^{I}$ redox couples, respectively. The two one-electron steps involved in the reduction of the metal centers were verified *via* chronoamperometry at E_{app} = −1.5 V *vs.* $Fc^{+/0}$ (Fig. S7(C) and S7(D)). Another two peaks at $E_{1/2}$ = −1.28 V *vs.* $Fc^{+/0}$ and $E_{1/2}$ = −1.52 V *vs.* $Fc^{+/0}$ in Fig. S6(D) correspond to reductions of the 8HQ and Tpy moieties of the 8HQ-Tpy ligand, respectively. Moreover, upon complexation the metal lowers the energy of the ligand's π^* orbitals *via* metal–ligand orbital interactions. This stabilization makes it thermodynamically difficult to add electrons, causing the ligand-based reduction peaks to shift to more negative (cathodic) potentials which is seen in Fig. 3(B).

Electrochemical CO_2 reduction

The electrocatalytic CO_2 reduction by **[Co1]** was studied in DMF containing 0.1 M $[NBu_4](ClO_4)$ as supporting electrolyte under saturated CO_2 conditions, with H_2O as the proton source. The hydration of CO_2 forms H_2CO_3, which acts as a proton source in the presence of water. According to experimental measurements, the pH of the solution (4.8 mL DMF + 0.2 mL H_2O) was 10.2 prior to the addition of CO_2 and 7.1 following CO_2 saturation. These pH values correspond to free proton concentrations 6.31 × 10^{-11} M and 7.94 × 10^{-8} M, respectively. The observed pH drop is compatible with partial protonation of the base by CO_2-derived H_2CO_3, according to the pK_a of H_2CO_3 in DMF (7.37).[43] The measured values demonstrate considerable protonation reflecting the expected action of CO_2 in DMF/4% H_2O. No changes were observed in the metal-based peaks in cyclic voltammetry analyses of **[Co1]** in a CO_2-saturated solution (Fig. 4A). Moreover, the addition of 2.2 M (*i.e.* 200 μL) of H_2O under N_2 atmosphere does not signify any increment in the catalytic current due to proton reduction. However, a significant increase in the catalytic current was observed under saturated CO_2 conditions, with onset potentials of −2.07 V *vs.* $Fc^{+/0}$ (Fig. 4B). The current increased slightly further in the cathodic direction with the addition of 2.2 M of H_2O as the proton source at a scan rate of 0.1 V s^{-1} (Fig. 4B). This electrocatalytic feature reveals that CO_2 reduction reactions (CO_2RR) are a faster process than the hydrogen evolution reaction (HER), which has been further verified by controlled potential electrolysis (*vide infra*). Savéant *et al.* proposed a method to determine the standard potential ($E^{o\prime}$) for the CO_2 to CO reduction based on the thermodynamic cycle of reductive reactions. The standard potential for CO_2-to-CO, $E^{0\prime}_{CO_2/CO,DMF}$ = −1.45 *vs.* $Fc^{+/0}$ (pK_a value of 7.37 for H_2CO_3 in DMF).[43a] Accordingly, **[Co1]** produces CO from CO_2 at an overpotential of 760 mV *vs.* $Fc^{+/0}$, with catalytic mid-wave potentials ($E_{cat/2}$) at −2.23 V *vs.* $Fc^{+/0}$, at a scan rate of 0.1 V s^{-1}.[44]

Catalysis only starts once both cobalt centres are reduced to the +1 oxidation state, which is followed by the reduction of the 8HQ ligand, according to cyclic voltammetry conducted in a CO_2 environment. The fully reduced [Co(I)Co(I)(8HQ$^{\bullet-}$-Tpy)] complex is the catalytically active species, according to this sequence. The requirement for this ligand-centered reduction suggests that the 8HQ unit plays a significant part in promoting CO_2 activation, either by enhancing nucleophilicity or *via* electronic delocalization through metal–ligand cooperativity. These results are consistent with the observed low kinetic isotope effect (k_H/k_D = 1.17, *vide infra*) and little hydrogen evolution activity, suggesting an EECC-type process in which several electron accumulation stages precede CO_2 binding and protonation.

Controlled potential electrolysis

Controlled potential electrolysis (CPE) experiments were carried out using 5.0 mL of a 0.50 mM solution of **[Co1]** in a DMF/H_2O mixture (4.8 : 0.2 v/v). The experiments were per-

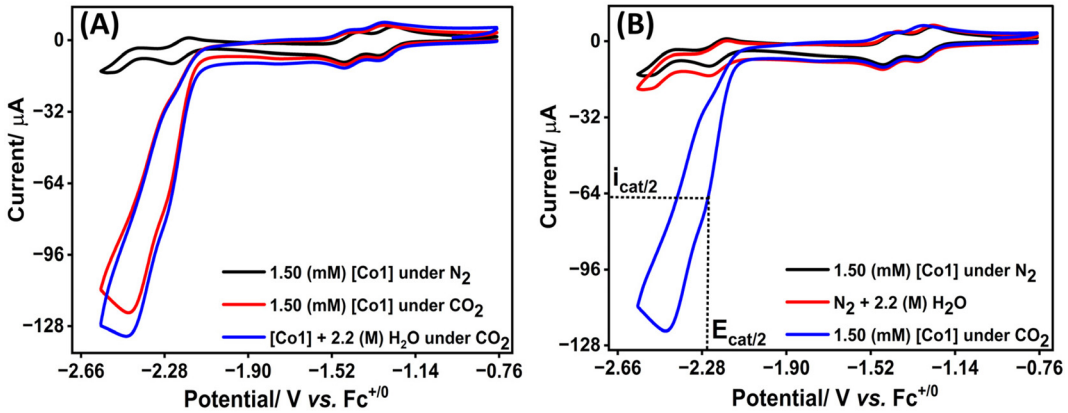

Fig. 4 Cyclic voltammograms of (A) 1.50 mM **[Co1]** in DMF using 0.1 M $[NBu_4](ClO_4)$ as supporting electrolyte under N_2, N_2 with 2.2 M H_2O and CO_2 atmosphere (B) 1.50 mM **[Co1]** complex in DMF under N_2, CO_2, and N_2 with 2.2 M H_2O.

formed in a custom-made electrolyzer with 0.1 M $[NBu_4](ClO_4)$ as the supporting electrolyte, applying potentials ranging from −2.0 V to −2.3 V *vs.* $Fc^{+/0}$ (Fig. S8A). As the applied potential increased, the charge accumulation also increased (Fig. S8A). After 2.0 h of electrolysis, a rinse test was conducted on **[Co1]**, followed by a CPE experiment without the complex at −2.3 V *vs.* $Fc^{+/0}$. No gaseous products were detected in the bulk electrolysis without a catalyst or in the rinse test (Fig. S8B). Additionally, NMR spectra of the solution of **[Co1]** after 2.0 h of electrolysis did not exhibit any peaks attributable to the $HCOO^-$ ion.

Gaseous products, including CO and H_2, were detected by gas chromatography using a flame ionization detector (FID) and a thermal conductivity detector (TCD). The retention times and the calibration plots of standard CO and H_2 gases are provided in Fig. S9 and S10, respectively. Gas chromatography plots for CO_2 reduction by **[Co1]** at −2.0 V to −2.3 V *vs.* $Fc^{+/0}$ are displayed in Fig. S11 and S12. After 2.0 h of electrolysis, gaseous samples were collected using a gas-tight syringe and injected into the GC. The amounts of CO and H_2 produced were quantified using the calibration plot. The quantities of CO and H_2 generated at each potential during electrolysis are presented in Fig. 5.

Furthermore, the gaseous products were confirmed using an online Mass Analyzer equipped with an Omni StarTM Mass Analysis System GSD 320 (Pfeiffer) quadrupole mass spectrometer apparatus. In addition, a labeling experiment was conducted using an online gas analyzer to identify $^{12}CO_2$ and $^{13}CO_2$ molecules.[45,46] The gas analyzer sensor was attached to the headspace of the electrochemical cell during CPE.

During electrolysis, the evolution of H_2 was initially detected ahead of CO, indicating the consecutive reduction of protons to H_2 followed by the reduction of CO_2 to CO. The detection of H_2, ^{12}CO, and ^{13}CO (H_2, m/z = 2; ^{12}CO, m/z = 28; and ^{13}CO, m/z = 29) during controlled potential electrolysis of **[Co1]** under $^{12}CO_2$ and $^{13}CO_2$ atmosphere is depicted in Fig. S13 and Fig. 6.

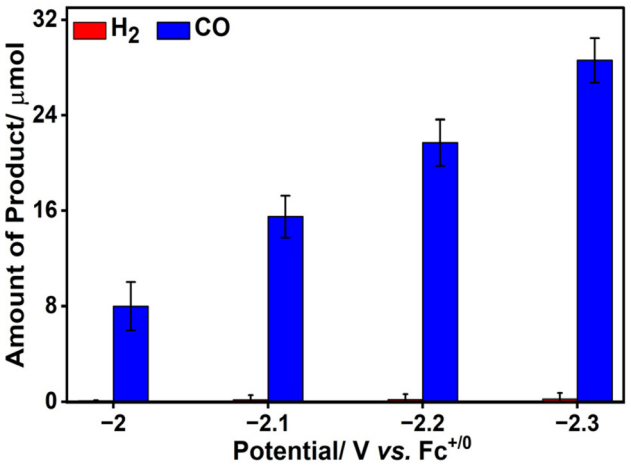

Fig. 5 Amount of CO and H_2 produced after 2.0 h of CPE at different potentials ranging from −2.0 V to −2.3 V *vs.* $Fc^{+/0}$ for **[Co1]** complex.

The Faradaic Efficiency (FE) for CO evolution for the **[Co1]** complex was determined to be 94 ± 2% at −2.2 V *vs.* $Fc^{+/0}$ (Fig. 7). In comparison, the Faradaic efficiencies (FE) for H_2 evolution for the same complex were calculated to be 1.00% at −2.0 V *vs.* $Fc^{+/0}$ after 2.0 h of electrolysis (Fig. 7). The TONs and TOFs for CO_2 reduction by **[Co1]** after 2 h of CPE at different potentials are summarized in Tables S4 and S5. A comparison with the reported mononuclear and dinuclear Co-based catalysts are provided in Table 1.

Catalyst stability

Catalyst stability is of utmost importance in electrochemical CO_2 reduction reactions (CO_2RR). UV-Visible spectroscopy and cyclic voltammetry were employed to evaluate the stability of **[Co1]** under operating conditions. Spectra were recorded before and after bulk electrolysis of 0.050 mM of **[Co1]** in a DMF and 2.2 M H_2O mixture (Fig. S14A). Remarkably, the spectra showed no significant changes under catalytic con-

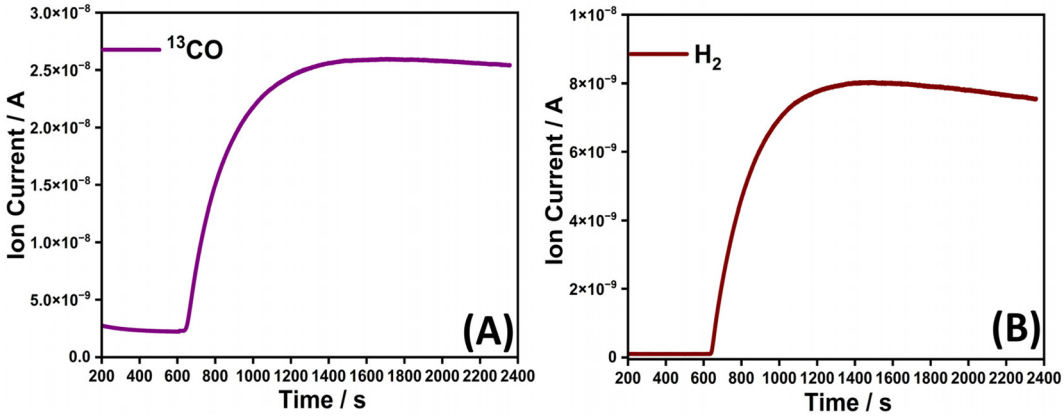

Fig. 6 The controlled potential electrolysis of $[Co(8HQ\text{-}Tpy)(H_2O)]_2(PF_6)_2$; **[Co1]** as catalyst under $^{13}CO_2$ (A) ^{13}CO detection, (B) H_2 detection by online mass analyzer.

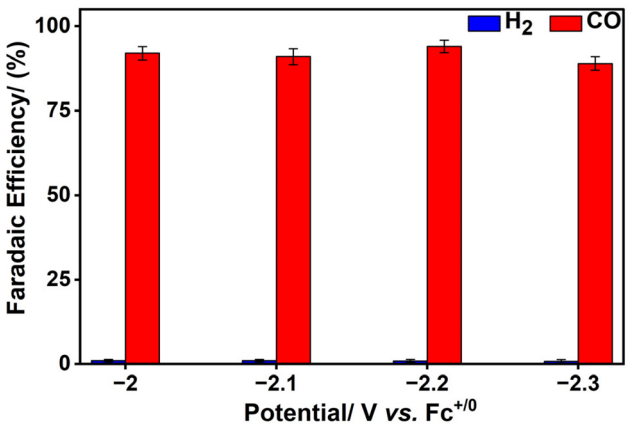

Fig. 7 Faradaic efficiency of CO and H_2 production after 2.0 h of CPE at potentials varying from −2.0 V to −2.3 V *vs.* $Fc^{+/0}$ for **[Co1]**.

ditions, indicating significant robustness of the complex. Additionally, cyclic voltammetry experiments provided supporting data for homogeneous reaction kinetics (Fig. S14B). After 2.0 hours of electrolysis, a rinse test was conducted for **[Co1]** (Fig. S8B), confirming the homogeneous nature of the catalytic conditions and the stability of **[Co1]** throughout the catalytic process. To further assess the homogeneity and stability of the complex during the catalytic process, ESI-mass spectra (Fig. S15) were recorded before and after CPE of **[Co1]** at −2.3 V *vs.* $Fc^{+/0}$. The ESI mass spectra show a very minute shift in peak positions before and after electrolysis, which implies that the complex was stable and homogeneous during the electrolytic conditions.

The cyclic voltammetry experiments further confirmed the homogeneous nature of the reaction. For a better understanding of the homogeneity and stability of the complex during the catalytic process, Scanning Electron Microscopy (SEM) (Fig. S16 and S17), and Energy-Dispersive X-Ray Spectroscopy (EDX) (Fig. S18 and S19) analysis were carried out on the working electrode surface, specifically the glassy carbon plate. Controlled potential electrolysis was performed for 2.0 hours using 0.1 M $[NBu_4](ClO_4)$ as the electrolyte for the blank experiment (without catalyst) and, in another experiment, with the **[Co1]** complex at an applied potential of −2.2 V *vs.* $Fc^{+/0}$. SEM

Table 1 Comparison with the reported mononuclear and dinuclear Co-based catalysts

Catalyst system	FE(CO)	FE(H_2)	Main product(s)	Design principle	Ref.
$[Co(tpy)_2]^{2+}$	31%	23%	CO + H_2	Ligand-tuned redox behavior	32*b*
$[Co(DBPy\text{-}PyA)]^{2+}$	~6%(CO) +7% HCOOH	78%	H_2	Coordination geometry control	33*a*
Capsule-like Co complex	~90%	<10%	CO	Proton management *via* cavity control	33*b*
$[Co^{II}(TPA)Cl][Cl]$	TON > 900	—	CO	Rigid ligand architecture	33*c*
$[Co(N_5)]^{2+}$	~82%	Low	CO	Metal–ligand electronic interplay	33*d*
$[Co(qpy)(OH_2)_2]^{2+}$	94%	1%	CO	Extended quaterpyridine system, enhanced redox stability/selectivity	33*e*
$[Co_2(biqpy)Cl]^{3+}$	~90%(CO) +7%(HCOOH)	0.5%	CO	Bimetallic synergy for activation	36
$[Co(8HQ\text{-}Tpy)(H_2O)]_2(PF_6)_2$	94%	1%	CO	Asymmetric metal–ligand cooperation	This work

DBPy-PyA = (1-([2,2′-bipyridin]-6-yl)-*N*-([2,2′-bipyridin]-6-ylmethyl)-*N*-(pyridin-2-ylmethyl) methanamine; TPA = tris(2-pyridylmethyl)amine; N5 ligand (2,13-dimethyl-3,6,9,12,18-pentaazabicyclo[12.3.1]octadeca-1(18),2,12,14,16-pentaene); qpy = 2,2′:6′,2″:6″,2‴-quaterpyridine); biqpy = 4,4″ ″-(2,7-di-*tert*-butyl-9,9-dimethyl-9*H*-xanthene-4,5-diyl)di-2,2′:6′,2″:6″,2‴-quaterpyridine.

and EDX analyses revealed only trace amounts of cobalt metal deposited on the working electrode surface after electrolysis, more precisely 0.08 atom% for the **[Co1]** complex under the specified reaction conditions, indicating a homogeneous nature of the catalysis effected by **[Co1]**. Moreover, from XPS studies, it has also been confirmed that deposition of metal catalyst does not occur on the electrode surface upon performing CPE for 2.0 h in a CO_2 atmosphere using 0.5 M **[Co1]** complex (Fig. S20).

Electrode surface phenomena

Cyclic voltammetry is a robust electroanalytical technique for elucidating the complexities of molecular catalysis and its underlying mechanisms. Particularly in the context of CO_2 reduction, this method allows for extracting crucial parameters such as CO_2 binding rates, equilibrium constants, kinetics of intermediate steps, and the reaction order concerning catalyst, CO_2, and proton source. In this study, the catalytic kinetics exhibited by the **[Co1]** complex was systematically explored using various regimes encompassing catalyst concentration from 0.50 mM to 2.50 mM, water dependence (ranging from 0.55 M to 2.20 M), and scan rate dependence varying from 0.1 V s^{-1} to 1 V s^{-1}. This comprehensive approach necessitated a re-evaluation of dependencies within each regime.

A Cottrell plot, which shows the peak current *versus* the square root of the scan rate ($\nu^{1/2}$) for the $Co^{II}Co^{II}/Co^{II}Co^{I}$ and $Co^{II}Co^{I}/Co^{I}Co^{I}$ redox processes, was found to be linear for **[Co1]**. This observation was made during cyclic voltammetry experiments conducted with 1.0 mM solutions of complex in DMF under N_2 or CO_2 atmospheres, with scan rates ranging from 0.025 to 0.25 V s^{-1} (Fig. S21 and S22). The diffusion coefficients for the $Co^{II}Co^{II}/Co^{II}Co^{I}$ and $Co^{II}Co^{I}/Co^{I}Co^{I}$ redox events under N_2 were determined for the cathodic peaks $D_{0,c}$ = 0.6×10^{-6} and 1×10^{-6} cm^2 s^{-1}, respectively. For the anodic peak, the diffusion coefficients were $D_{0,a} = 0.3 \times 10^{-6}$ and 0.25×10^{-6} cm^2 s^{-1}, respectively. These values indicate that the redox events were diffusion-controlled and homogeneous in DMF solution under a nitrogen atmosphere. Similarly, diffusion-controlled behaviour was observed for the $Co^{II}Co^{II}/Co^{II}Co^{I}$ and $Co^{II}Co^{I}/Co^{I}Co^{I}$ redox events under a CO_2 atmosphere (Fig. S21 and S22). The diffusion coefficients for the cathodic peak under CO_2 were $D_{0,c} = 0.8 \times 10^{-6}$ and 1.4×10^{-6} cm^2 s^{-1}, respectively. The diffusion coefficients for the anodic peak under CO_2 were $D_{0,a} = 0.3 \times 10^{-6}$ and 0.5×10^{-6} cm^2 s^{-1}, respectively. These values indicate that the redox events were diffusion-controlled and occur uniformly in DMF solution under a CO_2 atmosphere.

Subsequently, cyclic voltammograms were recorded by varying scan rate from 0.1 V s^{-1} to 1.5 V s^{-1} in DMF medium under N_2 and CO_2 atmosphere (Fig. S23). The plateauing of the catalytic current at scan rates beyond 1.0 V s^{-1} can be attributed to kinetic limitations of the CO_2 reduction reaction at the electrode surface. At lower scan rates, the current increases proportionally because the reaction is under diffusion-controlled conditions. However, at higher scan rates (>1.0 V s^{-1}), the system becomes electron-transfer limited, and the mass transport of CO_2 to the electrode surface cannot keep up with the faster potential sweep. This results in a saturation of the catalytic current (Fig. S23B and S24). Moreover, TOF has been extracted for each scan rate using the equation;[47]

$$\frac{i_p}{i_{cat}} = \frac{1}{0.446}\sqrt{\frac{RTk_{obs}}{nF\upsilon}}$$

{where, R = universal gas constant; T = temperature; n = number of electrons involved; F = Faraday's constant; υ = scan rate; k_{obs} = rate constant}. Using this equation actual rate constant (TOF_{max}) of the catalyst **[Co1]** has been calculated in CO_2 saturated atmosphere and found to be 2575.0 s^{-1} (Fig. 8).

Investigations into the kinetics of electrocatalytic CO_2 reduction involved analyzing the catalytic cyclic voltammograms of the **[Co1]** complex. The rate of CO_2 reduction was enhanced upon rising catalyst concentrations, following a linear trend. According to the equation $i_{cat} = n_{cat}FA[cat](Dk_{CO_2}[CO_2])^{1/2}$, there is a first-order dependence of catalytic activity on catalyst concentration (Fig. S25(A) and S25(B)).

Moreover, the catalytic current exhibits a linear dependence on the concentration of H_2O. The choice of proton source in electrochemical CO_2 reduction was crucial for determining the efficiency, selectivity, and overall effectiveness of the reaction. Acidic environments, for example, enhance the protonation of intermediates like H_2CO_3, formed during CO_2 reduction, thereby accelerating the reaction rates. Such conditions were essential for optimizing the efficiency of CO_2 conversion to the desired products. In this study, we varied the H_2O concentration up to 2.2 M to serve as a proton source that participates in the rate-determining steps (Fig. S26(A) and S26(B)).

Analyzing the kinetic isotope effect (KIE) by monitoring the catalytic current (i_{cat}/i_p) at different H_2O and D_2O concentrations revealed a linear relationship with proton donor concentration (Fig. S27). The **[Co1]** complex exhibited a modest KIE value of 1.17 ± 0.05, suggesting that proton transfer is not the rate-limiting step. An EECC-type mechanism, in which electron accumulation comes before CO_2 activation and sub-

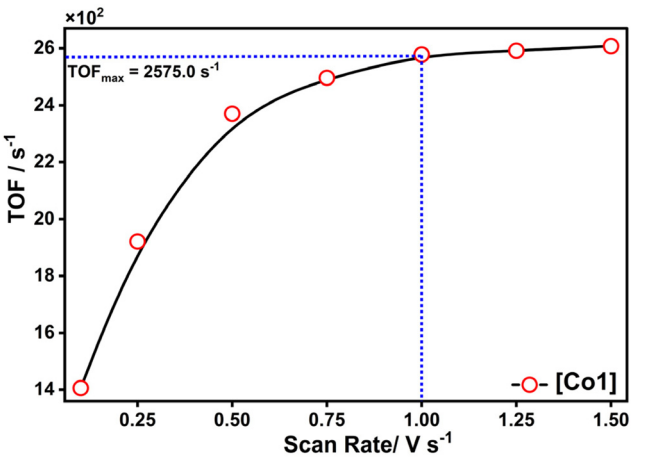

Fig. 8 Plot of TOF *vs.* scan rate for the calculation of TOF_{max} for catalyst **[Co1]** under CO_2 saturated atmosphere in DMF medium.

sequent protonation, is supported by this minor isotope effect as well as electrochemical evidence that catalysis only starts after complete reduction of both cobalt centres and the 8HQ ligand. In accordance with metal–ligand cooperativity, the 8HQ moiety of the ligand most likely promotes CO_2 binding through increased nucleophilicity or electronic delocalization. Although the proton source is necessary to complete the catalytic cycle, its limited kinetic contribution indicates that the chemical step that limits turnover is CO_2 binding or C–O bond cleavage.

Spectroelectrochemistry

The system was further studied by UV-Visible spectroelectrochemical measurements (UV-SEC). In these experiments, 0.18 mM of **[Co1]** was electrochemically reduced using 0.1 M $[NBu_4](ClO_4)$ as the supporting electrolyte at −2.3 V *vs.* $Fc^{+/0}$ under N_2 and CO_2 atmospheres (Fig. 9). During the UV-SEC experiment, the band intensity increases in the visible region. It occurs when **[Co1]** is reduced at a particular potential, correlating with changes in the UV-Vis absorbance spectra. The band intensity increases at 586 nm (ε = 2800 M^{-1} cm^{-1}; for each Co metal center ε = 1400 M^{-1} cm^{-1}) due to the formation of a Co(I) species, which is crucial for CO_2 activation, and corresponds to a d–d transition band. The reduced **[Co1]** interacts with CO_2, leading to the formation of an intermediate complex. The intermediate undergoes protonation and further reduction steps, ultimately forming reduced carbon species such as CO.

Infrared spectroelectrochemical (IR-SEC) measurements (Fig. 10(A)) were performed in a sealed OTTLE cell with CaF_2 windows, using a Pt mesh working electrode, Pt wire auxiliary, and Ag wire pseudo-reference. A 0.5 mM complex solution in 5 mL of DMF/H_2O (4.8 : 0.2 v/v) with 0.1 M TBAP was purged with N_2, then CO_2 for 15 min, and electrolysis was conducted at −2.3 V *vs.* $Fc^{+/0}$. The emergence of a deprotonated CO_2-derived intermediate, such as M–CO_2^- or formate, is indicated by the IR bands seen at 1670 and 1388 cm^{-1} during electrolysis under CO_2 (Fig. 10(B)).[37,47b–d] Fig. 10(C) presents the ΔTransmittance (normalized) *vs.* wavenumber plot, showing the difference between spectra recorded during electrolysis

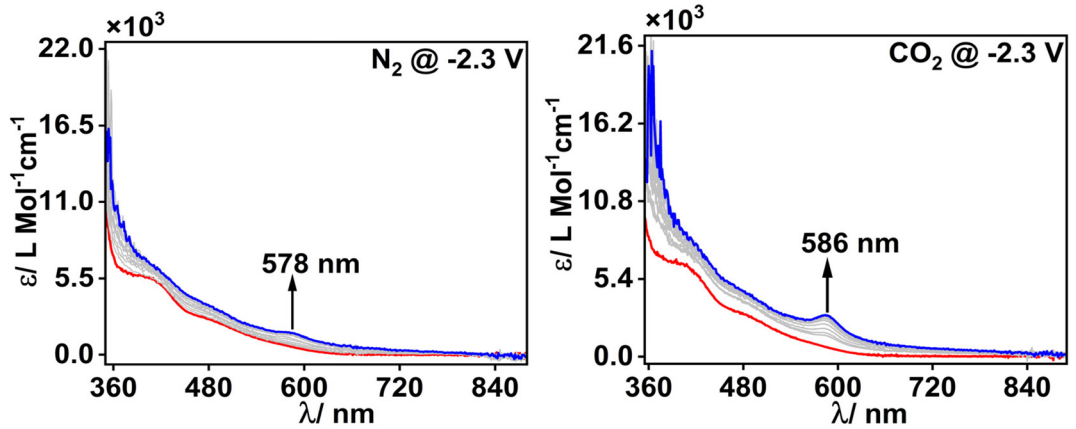

Fig. 9 Spectral changes during spectroelectrochemical studies for **[Co1]** at −2.3 V *vs.* $Fc^{+/0}$ using 0.1 M $[NBu_4](ClO_4)$ as supporting electrolyte under N_2 and CO_2 atmosphere.

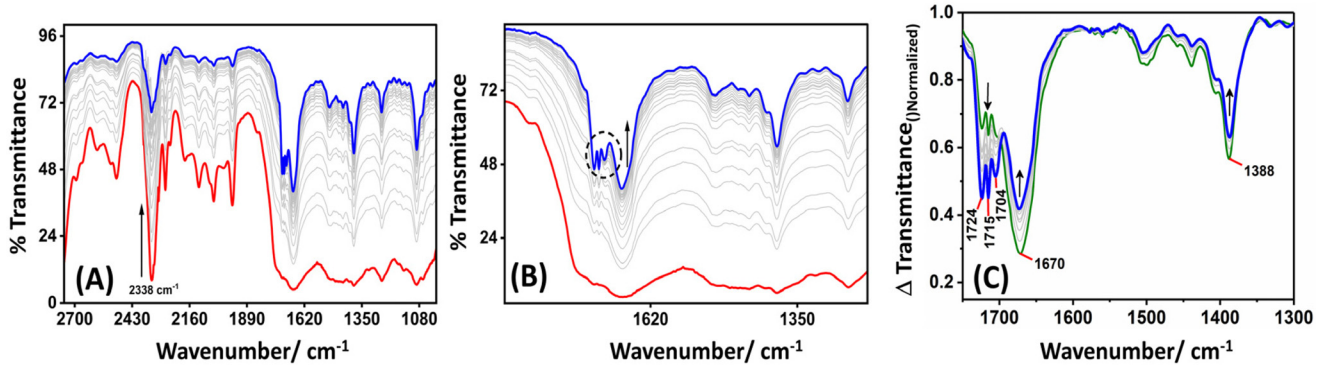

Fig. 10 (A) SEC-IR of 0.50 mM of **[Co1]** in DMF medium containing 0.1 M $[NBu_4](ClO_4)$ as a supporting electrolyte and 100 μL H_2O as proton source under CO_2 atmosphere (red color is the catalyst before electrolysis). (B) The enlarged region of SEC-IR spectra. (C) The $\Delta Transmittance_{(Normalized)}$ *vs.* wavenumber plot, where the initial spectra before electrolysis (red color in A and B) have been subtracted from the observed spectra during electrolysis.

and the initial pre-electrolysis spectrum, highlighting spectral changes associated with electrochemical transformations. These bands correspond to the asymmetric and symmetric stretching modes of the carboxylate group (ν_{asym} and ν_{sym} COO^-). These characteristics imply that CO_2 is first activated in its anionic form at the metal centre and then stabilised by coordination. As the reaction continues, additional bands that are indicative of C═O stretching vibrations in protonated carboxylic acid species (M–CO_2H) progressively appear at 1704, 1715, and 1724 cm^{-1} (Fig. 10(C)). A shift from a loosely linked or deprotonated intermediate to a more distinct, protonated species is reflected in this spectral development. Collectively, these findings demonstrate the dynamic coordination environment at the metal centre under catalytic circumstances and offer compelling evidence for a sequential method of CO_2 activation, including both anionic and protonated intermediates.

DFT calculations

The electrochemical CO_2 reduction reaction was computationally modelled by DFT calculations[48,49] performed using the Gaussian 16[50] program package (Scheme 2). Geometry optimization and frequency calculations of all intermediates were carried out based on B3LYP[51,52] functional, LANL2DZ[53] basis set for two Co metal centers and Pople's 6-31G[54,55] with consideration of polarization effect on the basis set for all other atoms (H, C, N, O). The solvent effect of dimethylformamide (DMF, ε = 36.71) in the reaction was considered by the self-consistent reaction field approach using the conductor-like polarizable continuum model (CPCM). Table S7 presents the calculated energies (in Hartree) of various intermediates and transition states in their most stable spin states. In the electrochemical CO_2 to CO formation reaction, experimental potential and pH are crucial to calculate free energy and reduction potential (detailed computational details are in the SI).[56] In this study, we implemented an experimental applied potential of −1.56 V (*vs.* SHE) and pH of 7.37 to construct a free energy profile. In **Int-1**, the Co metal centers are penta-coordinate with four nitrogen centers and one oxygen center. All intermediates are optimized from low spin to high spin electronic structure to decide the most stable geometry (Fig. S28).

The sextet state of **Int-1** is the most stable spin state of the molecule and is 9.4 kcal mol^{-1} and 10.6 kcal mol^{-1} more stable than the corresponding doublet and quartet states, respectively. In an aqueous medium, a water exchange reaction may occur with reduced intermediates and catalysts (Fig. S29). The DFT study indicates that the hexacoordinate Co aqua complexes are less stable than the corresponding pentacoordinate complexes. In addition, for the reduction from **Int-1** to **Int-2**, the H_2O–Co bond distance increases, and the formation of the corresponding pentacoordinate complex by reduction of the hexacoordinate Co aqua complex becomes more exothermic than the corresponding reduction of a pentacoordinate Co complex.

In the first step in the electrochemical reduction of CO_2 to CO, **Int-1′** is reduced, followed by water desorption to produce **Int-1** (E° = −0.44 V *vs.* SHE). Subsequently, **Int-1** captures one electron to form **Int-2** (E° = −0.60 V *vs.* SHE) *via* an exergonic step with a reaction energy of −22.1 kcal mol^{-1} (Scheme 2).

In the next step, **Int-2** is further reduced by one electron to form **Int-3** with a relatively higher reduction potential of −1.59 V (*vs.* SHE) and reaction energy values (0.7 kcal mol^{-1}) than the first and second reduction reactions. In the CO_2 reduction reaction, a competitive hydrogen evolution reaction is also possible. All feasible stepwise proton and electron addition reaction paths in a hydrogenation reaction and dehydrogenation *via* dissociation of O–H and Co–H were computationally modelled (Scheme S1). In the hydrogen evolution reaction, a proton addition reaction either takes place at the 8-hydroxyquinoline oxygen (to form **Int-7**) or at the cobalt ion (to form **Int-9**) in a competitive hydrogen evolution reaction. The formation of **Int-7** is thermodynamically favored relative to **Int-9** with respective reaction energies of −9.3 and −4.5 kcal mol^{-1} (Fig. 11). The HOMO–LUMO analysis indicates that the HOMO is primarily distributed on the quinoline, while the LUMO is located on the terpyridine fragment in **Int-1** (Fig. S30). Compared to **Int-1**, the reduced intermediate **Int-3** has a smaller HOMO–LUMO energy gap, which may facilitate protonation at the 8-hydroxyquinoline oxygen in **Int-3**.

A spin density distribution analysis was performed to study the protonation reaction steps. In **Int-3**, the spin densities are mainly located at Co, and the adjacent oxygen and nitrogen are symmetrically distributed between the two fragments (Fig. 12). In the proton addition reaction, the spin density of the participating oxygen decreases from 0.055 to 0.001 (Table S8) due to its direct participation in the protonation reaction.

In Scheme S1, the formation of **Int-7** from **Int-2** can proceed *via* two possible stepwise pathways: proton transfer followed by electron transfer (**PT** → **ET**) *i.e.*, $\mathbf{Int-2} \xrightarrow{H^+,\,-2.4\ kcal\ mol^{-1}} \mathbf{Int-10} \xrightarrow{e^-,\,-6.2\ kcal\ mol^{-1}} \mathbf{Int-7}$ or electron transfer followed by proton transfer (**ET** → **PT**), *i.e.*, $\mathbf{Int-2} \xrightarrow{e^-,\,+0.7\ kcal\ mol^{-1}} \mathbf{Int-3} \xrightarrow{H^+,\,-9.3\ kcal\ mol^{-1}} \mathbf{Int-7}$. In the **PT** → **ET** pathway, **Int-2** undergoes a proton transfer to form **Int-10** (ΔG = −2.4 kcal mol^{-1}), which is then reduced to form **Int-7** *via* an electron transfer (ΔG = −6.2 kcal mol^{-1}). Alternatively, in the **ET** → **PT** pathway, **Int-2** is first reduced to form **Int-3** (ΔG = +0.7 kcal mol^{-1}), which then undergoes proton transfer to generate **Int-7** (ΔG = −9.3 kcal mol^{-1}). The energy difference between **Int-10** and **Int-3** is relatively small (3.1 kcal mol^{-1}), suggesting that the CO_2 reduction reaction (CO_2RR) may initially follow an **ECEC** pathway starting from **Int-2**. However, as the reaction progresses, particularly after the reduction of **Int-2** to **Int-3**, it is likely to shift toward an **EECC** pathway. This mechanistic switch is supported by the fact that proton addition to **Int-3** is significantly more favorable (ΔG = −9.3 kcal mol^{-1}) compared to proton addition to **Int-2** (ΔG = −2.4 kcal mol^{-1}), as shown in Scheme S1. The enhanced protonation at **Int-3** can be attributed to its increased electron density relative to **Int-2**, which facilitates proton addition at the O^--center following reduction.

The reduced **Int-3** reacts with CO_2 and generates C-coordinated metal CO_2 complex **Int-4**. Fig. S31 suggests that

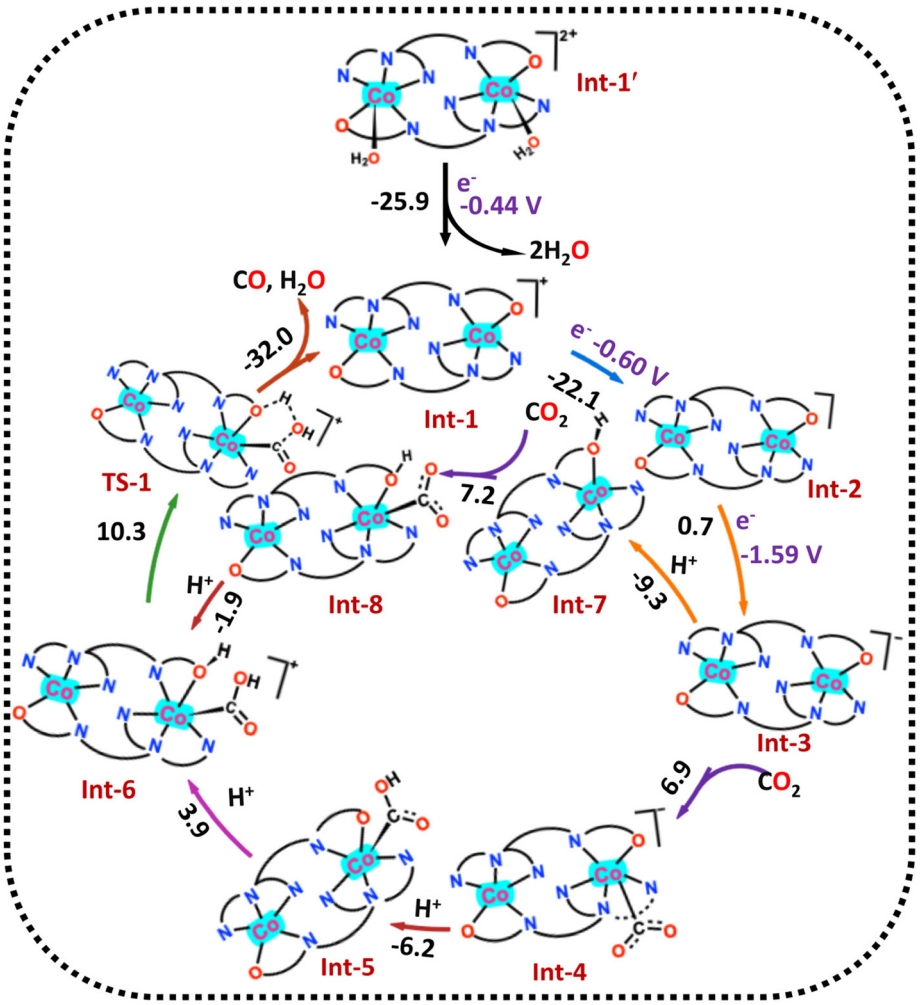

Scheme 2 The proposed reaction mechanism for Co metal-catalyzed CO_2 to CO formation reaction (free energy values in kcal mol^{-1} are shown in black color, and reduction potential values in V (*vs.* SHE) are shown in violet color).

with reduction, the Co metal center becomes more electron-rich, which in turn facilitates the CO_2 addition reaction with a 6.9 kcal mol^{-1} reaction energy. After CO_2 addition, the spin density at the participating Co metal center decreases from 2.551 to 1.072, indicating electron transfer from the metal to the CO_2 moiety. Eventually, one of the oxygen atoms of the CO_2 molecule **Int-4** can acquire one proton and convert to **Int-5**. The protonation at CO_2 is thermodynamically feasible with a reaction energy of −10.5 kcal mol^{-1} (Scheme 2). In the second protonation step, the oxygen atom of the 8-hydroxyquinoline entity receives a proton to make an O–H bond in **Int-6**. The proton addition step is energetically downhill by −0.4 kcal mol^{-1}.

In an alternative reaction pathway, the reduced intermediate **Int-3** can undergo protonation prior to CO_2 addition, leading to the formation of **Int-7**. Computational results suggest that protonation at the O^--center in **Int-3** is more favorable than CO_2 addition, with reaction energies of −9.3 kcal mol^{-1} and +6.9 kcal mol^{-1}, respectively. This indicates a stronger thermodynamic preference for protonation over CO_2 coordination at this stage. Subsequently, **Int-7** reacts with CO_2 to form **Int-8**, which, upon an additional protonation step, yields **Int-6**.

Further, the hydroxyquinoline O–H and formate C(=O)–OH bonds in **Int-6** dissociate through a five-membered transition state, **TS-1**, with an activation energy barrier of 10.3 kcal mol^{-1}. In **TS-1**, the C–O, O–H, and ligand O–H bond distances are elongated by 1.65 Å, 1.23 Å, and 1.18 Å, respectively, relative to their corresponding equilibrium bond lengths (Fig. S32). The transition state calculation was performed using the QST2 method without guessing the transition state and was further confirmed by the IRC calculation (Fig. 13). In the last step of the reaction, CO and H_2O dissociate to regenerate the active catalyst (**Int-1**) with a reaction energy of −32.0 kcal mol^{-1}.

In summary, the mechanistic DFT study suggests that upon reduction of the Co-center, coordinated water molecules dissociate from the metal complex, converting the hexa-coordinate

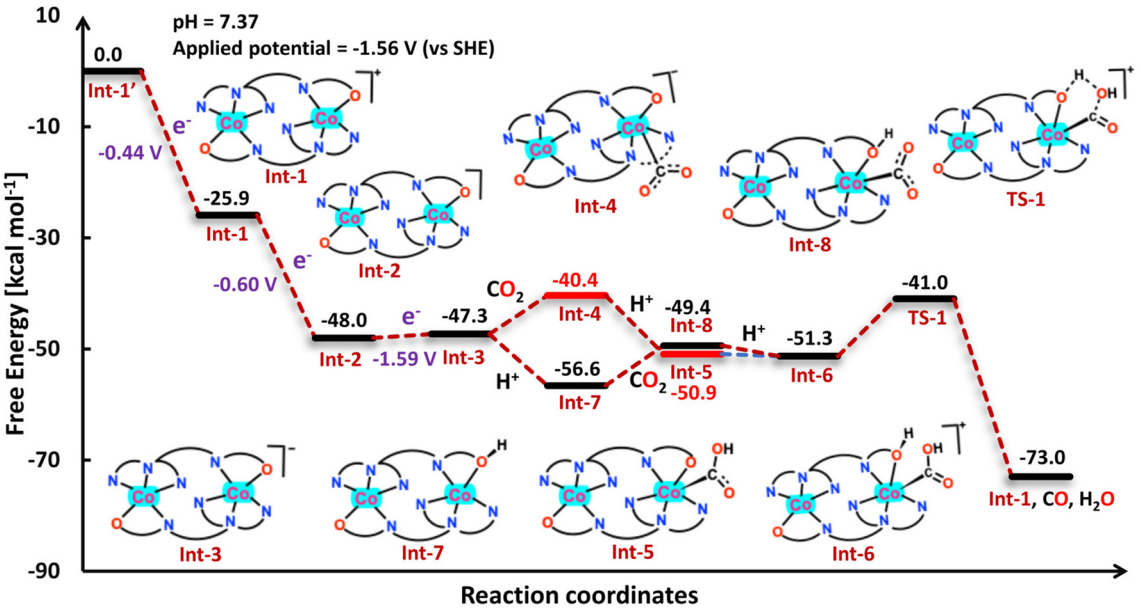

Fig. 11 Energy profile diagram for the proposed CO_2 reduction to CO formation reaction by Co-catalyst at pH = 7.37 and applied potential of −1.56 V (free energy values in kcal mol^{-1} are shown in black color, and reduction potential values in V *vs.* SHE is shown in violet color).

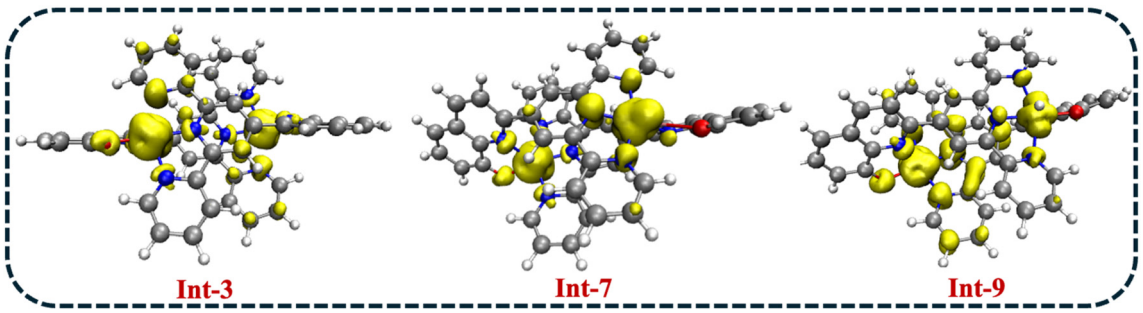

Fig. 12 Spin density distributions for **Int-3**, **Int-7**, and **Int-9** (with iso values of 0.003).

species into a penta-coordinate one. The catalytic CO_2 reduction reaction (CO_2RR) proceeds *via* initial reduction of the Co-based catalyst, followed by protonation at the ligand O^--center. In the stepwise proton and electron addition process, the reaction initially follows an ECEC pathway. However, due to the high proton affinity of the oxygen center in **Int-3**, formed after reduction of **Int-2**, the mechanism may shift to an EECC pathway, as supported by both experimental observations and DFT calculations. After the formation of **Int-3**, the most favorable pathway involves protonation of the Co-bound O^--center prior to CO_2 coordination. Subsequent CO_2 addition and a final protonation step led to the formation of CO and H_2O, with a relatively low activation energy barrier of 10.3 kcal mol^{-1}.

Correlation of DFT and experimental studies

An EECC-type mechanism for CO_2 reduction by the fully reduced [Co(I)Co(I)8HQ$^{\bullet-}$-Tpy] species is supported by DFT calculations. Significant delocalization is shown across both Co centres and the 8HQ moiety at full reduction, according to spin density studies. The deprotonated oxygen (O^-) of the 1e$^-$ reduced 8HQ-Tpy ligand exhibits a notable spin density (0.055), suggesting that it is involved in electronic communication and has redox activity. This spin density sharply drops to 0.001 upon protonation, indicating that this location is directly involved in the initial chemical process.

Protonation of the reduced deprotonated 8HQ oxygen is more advantageous than CO_2 coordination at **Int-3**, according to thermodynamic data, suggesting that protonation takes place before CO_2 binding. This sequence of stepwise reduction, protonation, and CO_2 activation is compatible with a mechanism of the EECC type. Further evidence that proton transfer is not the rate-limiting step and that CO_2 binding or subsequent bond cleavage most likely controls the total catalytic rate is provided by the experimentally found low kinetic isotope effect (k_H/k_D = 1.17).

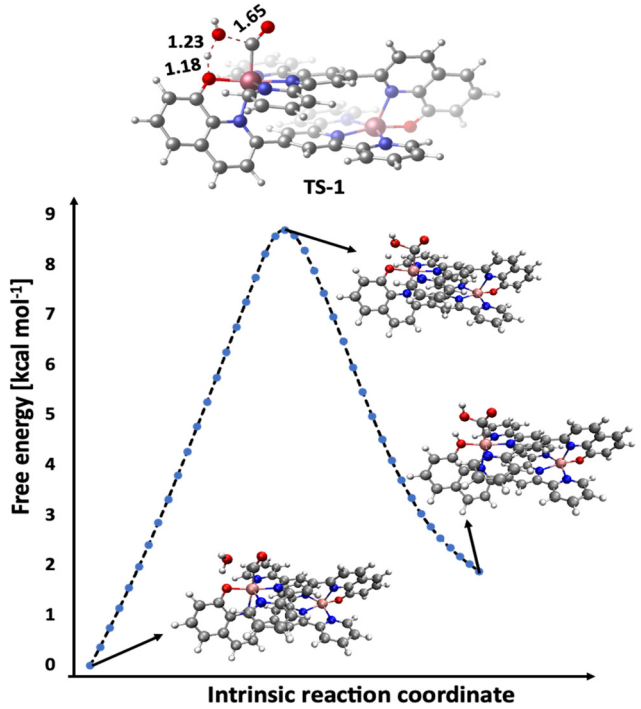

Fig. 13 Structure of transition state **TS-1** and corresponding intrinsic reaction coordinate path (all bond distances are in Å).

Conclusion

In a DMF/H_2O system, a novel cobalt-based electrocatalyst, [Co(8HQ-Tpy)$(H_2O)]_2(PF_6)_2$ (**[Co1]**), was developed for the selective electrochemical reduction of CO_2 to CO. **[Co1]** demonstrated great CO selectivity (Faradaic efficiency = 94 ± 2% and 99% selectivity) and excellent activity (TOF_{max} = 2575 s^{-1}) under electrolysis with 2.2 M water at an overpotential (760 mV). Gas analysis verified that CO was the primary product, with only a slight evolution in H_2. The CO_2 reduction occurs through ECEC-to-EECC pathways, involving consecutive proton and electron transfers, as determined by mechanistic and DFT investigations. A penta-coordinate intermediate is created when coordinated H_2O dissociates during reduction. With protonation at the Co–O^- site preferred to CO_2 binding (−9.3 *vs.* +6.9 kcal mol^{-1}), protonation and subsequent reduction result in **Int-3**. After that, CO and H_2O are released as the reaction moves through the low-barrier transition state **TS-1** (10.3 kcal mol^{-1}). Bands consistent with both protonated (M–CO_2H) and deprotonated (M–CO_2^-) intermediates are visible in IR-SEC spectra, suggesting gradual CO_2 activation. The rate may be limited by CO_2 coordination or bond breakage rather than proton transfer, as indicated by a modest kinetic isotope effect (k_H/k_D = 1.17).

Collectively, electrochemical, spectroscopic, and computational data support the idea that **[Co1]** predominantly operates through an EECC-type mechanism, providing important information for creating effective CO_2-to-CO molecular catalysts in moderate environments.

Author contributions

SkSA: conducted most of the experiments and wrote the initial draft. KM: conducted the theoretical studies and wrote the manuscript. DR: conducted experiments. MR: synthesized the complex and collected the crystal data. TNM: conducted labeled $^{13}CO_2$ studies. BSM: provided the resources for the DFT calculations and modified the manuscript. PB: help during labelling experiment. PK: provided the resources for online gas and mass analysis and labeled $^{13}CO_2$ studies. EN: conceived the idea and modified the draft manuscript. SKP: conceived the idea, provided the resources, and wrote and modified the draft manuscript.

Conflicts of interest

There are no conflicts to declare.

Abbreviations

CO_2RR	CO_2 reduction reaction
CPE	Controlled potential electrolysis
DFT	Density functional theory
FE	Faradaic efficiency
GC	Gas chromatography
HER	Hydrogen evolution reaction
SEM/EDX	Scanning electron microscopy with energy dispersive X-ray spectroscopy
SEC	Spectroelectrochemistry
SQUID	Superconducting quantum interference device
TBAP	Tetra butyl ammonium perchlorate
ILCT	Intra ligand charge transfer
MLCT	Metal-to-ligand charge transfer
PCET	Proton-coupled electron transfer
ECEC	Electron transfer–chemical reaction–electron transfer–chemical reaction
EECC	Electron transfer–electron transfer–chemical reaction–chemical reaction

Data availability

Supplementary information (SI): electronic spectra, HRMS, crystal data and refinement parameters, bond lengths, bond angles, magnetic, electrochemical, GC, SEM EDEX, XPS data and geometry-optimized coordinates.[57] See DOI: https://doi.org/10.1039/d5dt02003d.

Acknowledgements

This work was conducted at the Artificial Photosynthesis Laboratory, Department of Chemistry and Chemical Biology, IIT(ISM) Dhanbad, Jharkhand, India. SKP acknowledges the financial support by CSIR grant 01(3062)/21/

EMR-II. EN and SKP are thankful to STINT-INDIA initiation grant lnlB2022-9434. The authors acknowledge the CRF, IIT (ISM) Dhanbad for Single crystal XRD, HRMS, SEM/EDX, and XPS data. The SQUID data were collected from IIT Kharagpur. The theoretical studies were conducted at IIT Hyderabad. The online gas and mass analyses were conducted at IISER Tirupati.

References

1 K. Elouarzaki, V. Kannan, V. Jose, H. S. Sabharwal and J. M. Lee, *Adv. Energy Mater.*, 2019, **9**, 1900090.
2 C. Rosenzweig, D. Karoly, M. Vicarelli, P. Neofotis, Q. Wu, G. Casassa, A. Menzel, T. L. Root, N. Estrella, B. Seguin, P. Tryjanowski, C. Liu, S. Rawlins and A. Imeson, *Nature*, 2008, **453**, 353–357.
3 J. M. Saveant, *ChemElectroChem*, 2016, **3**, 1967–1977.
4 Z. Weng, J. Jiang, Y. Wu, Z. Wu, X. Guo, K. L. Materna, W. Liu, V. S. Batista, G. W. Brudvig and H. Wang, *J. Am. Chem. Soc.*, 2016, **138**, 8076–8079.
5 J. Qiao, Y. Liu, F. Hong and J. Zhang, *Chem. Soc. Rev.*, 2014, **43**, 631–675.
6 C. Costentin, M. Robert and J.-M. Savéant, *Acc. Chem. Res.*, 2015, **48**, 2996–3006.
7 A. M. Appel, J. E. Bercaw, A. B. Bocarsly, H. Dobbek, D. L. DuBois, M. Dupuis, J. G. Ferry, E. Fujita, R. Hille, P. J. A. Kenis, C. A. Kerfeld, R. H. Morris, C. H. F. Peden, A. R. Portis, S. W. Ragsdale, T. B. Rauchfuss, J. N. H. Reek, L. C. Seefeldt, R. K. Thauer and G. L. Waldrop, *Chem. Rev.*, 2013, **113**, 6621–6658.
8 K. E. Dalle, J. Warnan, J. J. Leung, B. Reuillard, I. S. Karmel and E. Reisner, *Chem. Rev.*, 2019, **119**, 2752–2875.
9 R. Francke, B. Schille and M. Roemelt, *Chem. Rev.*, 2018, **118**, 4631–4701.
10 J. Choi, P. Wagner, S. Gambhir, R. Jalili, D. R. MacFarlane, G. G. Wallace and D. L. Officer, *ACS Energy Lett.*, 2019, **4**, 666–672.
11 D. U. Nielsen, X. M. Hu, K. Daasbjerg and T. Skrydstrup, *Nat. Catal.*, 2018, **1**, 244–254.
12 M. E. Dry, *Catal. Today*, 2002, **71**, 227–241.
13 F. Jiao, J. Li, X. Pan, J. Xiao, H. Li, M. Ma, M. Wei, Y. Pan, Z. Zhou, M. Li, S. Miao, J. Li, F. Zhu, D. Xiao, T. He, J. Yang, F. Qi, Q. Fu and X. Bao, *Science*, 2016, **351**, 1065–1068.
14 S. Gonell, J. Lloret-Fillol and A. J. M. Miller, *ACS Catal.*, 2021, **11**, 615–626.
15 (*a*) S. Fukuzumi, Y.-M. Lee, H. S. Ahn and W. Nam, *Chem. Sci.*, 2018, **9**, 6017–6034; (*b*) K. Majee and S. K. Padhi, *New J. Chem.*, 2019, **43**, 3856–3865; (*c*) E. Ahmad, K. Majee, J. Patel, B. Das and S. K. Padhi, *Eur. J. Inorg. Chem.*, 2017, **2017**(28), 3409–3418; (*d*) S. K. Padhi, E. Ahmad and S. Rai, *Electrochim. Acta*, 2020, **340**(19), 136000; (*e*) M. Raj and S. K. Padhi, *New J. Chem.*, 2022, **46**(13), 6027–6038; (*f*) S. K. Padhi, E. Ahmad, S. Rai and B. Panda, *Polyhedron*, 2020, **187**, 114677.
16 K. Torbensen, B. Boudy, D. Joulié, N. von Wolff and M. Robert, *Curr. Opin. Electrochem.*, 2020, **24**, 49–55.
17 F. Franco, C. Rettenmaier, H. S. Jeon and B. R. Cuenya, *Chem. Soc. Rev.*, 2020, **49**, 6884–6946.
18 E. E. Benson, C. P. Kubiak, A. J. Sathrum and J. M. Smieja, *Chem. Soc. Rev.*, 2009, **38**, 89–99.
19 E. Boutin, L. Merakeb, B. Ma, B. Boudy, M. Wang, J. Bonin, E. Anxolabéhère-Mallart and M. Robert, *Chem. Soc. Rev.*, 2020, **49**, 5772–5809.
20 N. W. Kinzel, C. Werlé and W. Leitner, *Angew. Chem., Int. Ed.*, 2021, **60**, 11628–11686.
21 P. Saha, S. Amanullah and A. Dey, *Acc. Chem. Res.*, 2022, **55**, 134–144.
22 A. Bairagi, A. Y. Pereverzev, P. Tinnemans, E. A. Pidko and J. Roithová, *J. Am. Chem. Soc.*, 2024, **146**, 5480–5492.
23 P. L. Cheung, C. W. Machan, A. Y. S. Malkhasian, J. Agarwal and C. P. Kubiak, *Inorg. Chem.*, 2016, **55**, 3192–3198.
24 C. W. Machan, J. Yin, S. A. Chabolla, M. K. Gilson and C. P. Kubiak, *J. Am. Chem. Soc.*, 2016, **138**, 8184–8193.
25 M. D. Sampson and C. P. Kubiak, *J. Am. Chem. Soc.*, 2016, **138**, 1386–1393.
26 P. J. Chirik, *Acc. Chem. Res.*, 2015, **48**, 1687–1695.
27 F. W. Liu, J. Bi, Y. Sun, S. Luo and P. Kang, *ChemSusChem*, 2018, **11**, 1656–1663.
28 Z. Guo, S. Cheng, C. Cometto, E. Anxolabéhère-Mallart, S. M. Ng, C.-C. Ko, G. Liu, L. Chen, M. Robert and T. C. Lau, *J. Am. Chem. Soc.*, 2016, **138**, 9413–9416.
29 D. C. Lacy, C. C. L. McCrory and J. C. Peters, *Inorg. Chem.*, 2014, **53**, 4980–4988.
30 M. Zhang, M. El-Roz, H. Frei, J. L. Mendoza-Cortes, M. Head-Gordon, D. C. Lacy and J. C. Peters, *J. Phys. Chem. C*, 2015, **119**, 4645–4654.
31 H. Sheng and H. Frei, *J. Am. Chem. Soc.*, 2016, **138**, 9959–9967.
32 (*a*) N. Elgrishi, M. B. Chambers, V. Artero and M. Fontecave, *Phys. Chem. Chem. Phys.*, 2014, **16**, 13635–13644; (*b*) N. Elgrishi, M. B. Chambers and M. Fontecave, *Chem. Sci.*, 2015, **6**, 2522–2531.
33 (*a*) F. Droghetti, A. Amati, F. Pascale, A. Crochet, M. Pastore, A. Ruggi and M. Natali, *ChemSusChem*, 2024, **17**, e202300737; (*b*) A. Chapovetsky, T. H. Do, R. Haiges, M. K. Takase and S. C. Marinescu, *J. Am. Chem. Soc.*, 2016, **138**, 5765–5768; (*c*) K. T. Chan, M. Nippe, C. G. Margarit, R. Zong, H. M. Sayre, T. Zhang, V. S. Batista, G. W. Brudvig and R. H. Crabtree, *Chem. Commun.*, 2015, **51**, 10851–10854; (*d*) L. Chen, Z. Guo, X. Wei, C. Gallenkamp, J. Bonin, E. Anxolabéhère-Mallart, K. C. Lau, T.-C. Lau and M. Robert, *J. Am. Chem. Soc.*, 2015, **137**, 10918–10921; (*e*) Z. Guo, S. C. Cheng, C. Cometto, E. Anxolabéhère-Mallart, S.-M. Ng, C.-C. Ko, G. Liu, L. Chen, M. Robert and T.-C. Lau, *J. Am. Chem. Soc.*, 2016, **138**, 9413–9416.
34 (*a*) L. M. Cao, H. H. Huang, J. W. Wang, D. C. Zhong and T. B. Lu, *Green Chem.*, 2018, **20**, 798–803; (*b*) J.-H. Jeoung and H. Dobbek, *Science*, 2007, **318**, 1461–1464.
35 E. A. Mohamed, Z. N. Zahran and Y. Naruta, *Chem. Commun.*, 2015, **51**, 16900–16903.

36 Z. Guo, G. Chen, C. Cometto, B. Ma, H. Zhao, T. Groizard, L. Chen, H. Fan, W. L. Man, S. M. Yiu, K. C. Lau, T. C. Lau and M. Robert, *Nat. Catal.*, 2019, **2**, 801–808.
37 D. E. Polyansky, D. C. Grills, M. Z. Ertem, K. T. Ngo and E. Fujita, *ACS Catal.*, 2022, **12**, 1706–1717.
38 T. Ouyang, H. J. Wang, H. H. Huang, J. W. Wang, S. Guo, W. J. Liu, D. C. Zhong and T. B. Lu, *Angew. Chem., Int. Ed.*, 2018, **57**, 16480–16485.
39 B. D. Steffey, C. J. Curtis and D. L. DuBois, *Organometallics*, 1995, **14**, 4937–4943.
40 J. P. Du, A. Wilting and I. Siewert, *Chem. – Eur. J.*, 2019, **25**, 5555–5564.
41 W. Yang, S. S. Roy, W. C. Pitts, R. L. Nelson, F. R. Fronczek and J. W. Jurss, *Inorg. Chem.*, 2018, **57**, 9564–9575.
42 (*a*) M. Raj and S. K. Padhi, *Eur. J. Inorg. Chem.*, 2022, **2022**(21), e202200238; (*b*) S. K. Padhi and V. Manivannan, *Inorg. Chem.*, 2006, **45**, 7994–7996; (*c*) S. K. Padhi, R. Sahu and V. Manivannan, *Polyhedron*, 2008, **27**, 2221–2225; (*d*) S. K. Padhi, S. Rai and S. S. Akhter, *Inorg. Chem.*, 2020, **59**, 7810–7821; (*e*) M. Raj, K. Makhal, A. Mishra, B. S. Mallik and S. K. Padhi, *Inorg. Chem.*, 2023, **62**, 10993–11008; (*f*) M. G. Papanikolaou, A. Elliott, J. McAllister, J. K. Gallos, A. D. Keramidas, T. A. Kabanos, S. Sproules and H. N. Miras, *Dalton Trans.*, 2020, **49**, 15718–15730; (*g*) H. Sakiyama, *J. Comput. Chem., Jpn.*, 2007, **6**, 123–134; (*h*) H. Sakiyama, *Inorg. Chim. Acta*, 2006, **359**, 2097–2100; (*i*) H. Sakiyama, *Inorg. Chim. Acta*, 2007, **360**, 715–716; (*j*) H. Sakiyama, R. Ito, H. Kumagai, K. Inoue, M. Sakamoto, Y. Nishida and M. Yamasaki, *Eur. J. Inorg. Chem.*, 2001, **2001**(10), 2705–2713; (*k*) H. Sakiyama, R. Ito, H. Kumagai, K. Inoue, M. Sakamoto, Y. Nishida and M. Yamasaki, *Eur. J. Inorg. Chem.*, 2001, **2001**(8), 2027–2034.
43 (*a*) I. Azcarate, C. Costentin, M. Robert and J.-M. Savéant, *J. Phys. Chem. C*, 2016, **120**, 28951–28960; (*b*) S. S. Akhter, D. Srivastava, A. Mishra, N. Patra, P. Kumar and S. K. Padhi, *Chem. – Eur. J.*, 2024, **30**, e202403321; (*c*) S. S. Akhter and S. K. Padhi, *Eur. J. Inorg. Chem.*, 2022, **2022**(20), e202200206.
44 B. M. Stratakes, J. L. Dempsey and A. J. M. Miller, *ChemElectroChem*, 2021, **8**, 4161–4180.
45 S. Das, Kulbir, S. Ghosh and S. C. Sahoo, *Chem. Sci.*, 2020, **11**, 5037–5042.
46 S. Das and P. Kumar, *Dalton Trans.*, 2024, **53**, 6173–6177.
47 (*a*) E. S. Rountree, B. D. McCarthy, T. T. Eisenhart and J. L. Dempsey, *Inorg. Chem.*, 2014, **53**, 9983–10002; (*b*) S. C. Cheng, C. A. Blaine, M. G. Hill and K. R. Mann, *Inorg. Chem.*, 1996, **35**, 7704–7708; (*c*) P. Saha, S. K. Amanullah, S. Barman and A. Dey, *J. Am. Chem. Soc.*, 2025, **147**, 1497–1507; (*d*) A. A. Massie, C. Schremmer, I. Rüter, S. Dechert, I. Siewert and F. Meyer, *ACS Catal.*, 2021, **11**, 3257–3267.
48 W. Kohn and L. J. Sham, *Phys. Rev.*, 1965, **140**, A1133–A1138.
49 P. Hohenberg and W. Kohn, *Phys. Rev.*, 1964, **136**, B864–B871.
50 M. J. Frisch, *et al.*, *Gaussian 16, Revision C.01*, Gaussian, Inc., Wallingford CT, 2016.
51 C. Lee, W. Yang and R. G. Parr, *Phys. Rev. B: Condens. Matter Mater. Phys.*, 1988, **37**, 785–789.
52 A. D. Becke, *J. Chem. Phys.*, 1993, **98**, 5648–5652.
53 P. J. Hay and W. R. Wadt, *J. Chem. Phys.*, 1985, **82**, 270–283.
54 M. M. Francl, W. J. Pietro, W. J. Hehre, J. S. Binkley, M. S. Gordon, D. J. DeFrees and J. A. Pople, *J. Chem. Phys.*, 1982, **77**, 3654–3665.
55 W. J. Hehre, R. Ditchfield and J. A. Pople, *J. Chem. Phys.*, 1972, **56**, 2257–2261.
56 L.-L. Shi, M. Li, B. You and R.-Z. Liao, *Inorg. Chem.*, 2022, **61**, 16549–16564.
57 M. Raj and S. K. Padhi, CCDC 2449921: Experimental Crystal Structure Determination, 2025, DOI: 10.5517/ccdc.csd.cc2n7bqz.